applied sciences

MDPI

Article

A Novel Remote Sensing Image Enhancement Method, the Pseudo-Tasseled Cap Transformation: Taking Buildings and Roads in GF-2 as an Example

Jiqiu Deng [1,2], Wuzhou Dong [1,2], Yiwei Guo [1,2], Xiaoyan Chen [1,2], Renhao Zhou [1,2] and Wenyi Liu [3,4,*]

1 School of Geosciences and Info-Physics, Central South University, Changsha 410083, China
2 Key Laboratory of Metallogenic Prediction of Nonferrous Metals and Geological Environment Monitoring, Central South University, Ministry of Education, Changsha 410083, China
3 The Seventh Geological Team of Henan Nonferrous Metals Geological Bureau, Zhengzhou 450016, China
4 Henan Natural Resources Science and Technology Innovation Center (Multi-Source Remote Sensing Application Research), Zhengzhou 450016, China
* Correspondence: liuwenyicsugis@sina.com

Abstract: With the improvements in sensor accuracy, the spectral features of high-resolution remote sensing images become more complex. As a result, the classification accuracy for land cover classification decreases. Remote sensing image enhancements can improve the visual effect and the intra-class consistency and enhance the characteristics of ground objects. These enhancements are important for both image interpretation and improving image segmentation accuracy. In this study, we propose a pseudo-tasseled cap transformation (pseudo-TCT) through an orthogonal linear transformation of Gaofen-2 (GF-2) images using the untransposed tasseled cap transformation (TCT) coefficients, and further, enhance the visual effect and the separability among ground objects by linear stretching and percentage truncation stretching. To examine the separability among ground objects in the pseudo-TCT image, we used K-Means clustering, ISODATA clustering and 3D visualization of the spectral features of typical ground objects. The results show that the separability of buildings and roads from background objects is better than in the original image and the TCT image, and typical ground objects are effectively distinguished. Additionally, we visualized intra-class consistency by calculating the mean Euclidean distance between the pixel values of each point and the pixel values of its eight neighboring points and calculated the standard deviation of the intra-class consistency images. The results indicate that the secondary textures of the objects were weakened, and edges were made clearer, enhancing intra-class consistency. The pseudo-TCT is effective, at least in our work, and could be a candidate for image enhancement under certain applications.

Keywords: image enhancement; pseudo-TCT; GF-2; K-Means; intra-class consistency; buildings and roads

check for updates

Citation: Deng, J.; Dong, W.; Guo, Y.; Chen, X.; Zhou, R.; Liu, W. A Novel Remote Sensing Image Enhancement Method, the Pseudo-Tasseled Cap Transformation: Taking Buildings and Roads in GF-2 as an Example. *Appl. Sci.* **2023**, *13*, 6585. https://doi.org/10.3390/app13116585

Academic Editor: Jianbo Gao

Received: 12 March 2023
Revised: 22 May 2023
Accepted: 24 May 2023
Published: 29 May 2023

Copyright: © 2023 by the authors. Licensee MDPI, Basel, Switzerland. This article is an open access article distributed under the terms and conditions of the Creative Commons Attribution (CC BY) license (https://creativecommons.org/licenses/by/4.0/).

1. Introduction

Currently, the spatial resolution of remote sensing images has reached the sub-meter level, and the high-resolution images contain more spectral characteristics of ground objects. However, it also adds certain disturbing noise to the recognition and information extraction of some ground objects. For example, the variation of tree canopy due to light will be averaged out with the reduction of resolution, and the reduction of resolution can instead improve the inter-class separability [1,2]. This is because the images are enhanced, improving intra-class consistency and enhancing edges. Remote sensing image enhancement techniques can compress data and enhance features of ground objects, making the images easier to interpret manually or process by a machine. This is important for improving the segmentation accuracy of remote sensing images.

At present, the image enhancement techniques of remote sensing images are divided into three major categories: One is the spatial domain method, which focuses on point-to-point manipulation of the image; the second category is the frequency domain method. Fourier transforms are used to transform the image into the domain of spatial frequency; and the third category is color enhancement. Color enhancement techniques transform the grey-level image into color image models, such as RGB, HIS and CMY, and for remote sensing images, it is mainly the HIS Transform and Pseudo-Color Transform [3–6]. This study focuses on the spatial domain method, which is more concerned with point-to-point processing of remote sensing images, such as common NDVI, NDBI, linear stretching, PCA, TCT, etc. Recently, Zhao et al. proposed a deep learning fusion network DSLN that effectively utilizes NDVI to avoid the effects of few spectra, low inter-class separability and large intra-class variations in high-resolution images. The average OA and average Kappa coefficient of the classification accuracy reached 0.8069 and 0.7161, respectively, on the GF-1 dataset [7]. Gu et al. improved the NDBI and proposed the normalized spectral building index (NSBI) and differential spectral building index (DSBI), and both proposed indices achieved good enhancement results for different building conditions [8]. Furthermore, Yi and Jianhui addressed the problem of the low accuracy of urban impervious surface extraction by traditional linear spectral mixture analysis (LSMA) and improved LSMA by combining high-resolution remote sensing images, PCA and NDBI, and the improved LSMA extracted better accuracy of the impervious surface area [9]. Zeng et al. used BR-Net to train GF-2 images with PCA dimensionality reduction for building recognition and extraction, and not only is the recognition accuracy higher than the traditional machine learning model, but also the extracted buildings are more complete with clear boundaries [10].

TCT is an empirical orthogonal linear transformation of images made by Kauth and Thomas in 1976 and is based on the structure of the information distribution of the spectral information of soil and vegetation in multidimensional space, named because of the "tassel hat" shape of the spectra after the orthogonal linear transformation [11]. As the components formed by the TCT are not only independent of each other but also can better distinguish the main ground objects, the TCT is widely used in various fields. For instance, Chen et al. successfully extracted coastline using the greenness component and moisture component of the TCT with producer and user accuracy of 0.95 and 0.91, respectively, and higher accuracy for shorelines in areas with high sand content [12]. Liu et al. monitored the desertification process on the Mongolian plateau based on MODIS images processed by TCT and TGSI time series, which provided a new method for desertification research [13]. Chen et al. successfully achieved a high-precision extraction of water bodies using GF-1 images processed by TCT to attenuate the effects of shadows and dense vegetation [14]. Liu et al. combined TCT and support vector machines (SVMs) for land cover classification of Landsat 8 OLI images [15]. Li et al. used partial least squares regression (PLSR) to estimate the leaf area index (LAI) by adding the greenness component of TCT to achieve an estimate of LAI with a minimum number of features [16]. Chao et al. proposed a method to extract the flooded area of farmland based on TCT, to solve the low accuracy of traditional water body extraction methods due to the high-water content of crops after disasters [17]. The application of TCT has long gone beyond the initial proposal for crop growth monitoring, but the existing applications on TCT, although with high accuracy, lack controlled experiments.

The TCT uses the transpose of the TCT coefficients to achieve an orthogonal linear transformation of the image, while the orthogonal linear transformation of the image by the TCT coefficients without transposition and further enhanced by linear stretching and percentage truncation stretching (PTS) is the pseudo-TCT [18–22]. Currently, the assessment of the effects of image enhancement algorithms are mainly divided into two categories, one is the subjective image quality assessment (IQA), in which the image quality is observed and assessed manually; the other is the objective IQA, which uses algorithms to assess the image quality [23,24]. The objective IQA can be divided into three categories according to their

dependence on the high-quality (HQ) reference image: the first category is the full-reference (FR) IQA, using all the information of the HQ reference image for IQA; the second category is reduced-reference (RR) IQA, which only requires comparison with some statistical features of the HQ reference image; and the third category is no-reference (NR) IQA, which does not require the HQ reference image [25–31]. Bosse et al. proposed an NR IQA method based on a deep convolutional neural network (CNN). They evaluated the network on the LIVE database and achieved a liner Person correction that outperformed state-of-the-art reference image IQA methods [32]. Liu et al. developed an efficient general-purpose NR IQA model, dubbed spatial-spectral entropy-based quality (SSEQ) index [33]. Although FR IQA and RR IQA are easier to use and more sophisticated, the HQ images cannot be obtained as reference images in many cases. To test the effects of the pseudo-TCT, we also assessed the pseudo-TCT image quality from both subjective IQA and objective IQA.

Although the TCT coefficients of IKONOS were proposed in 2003, its property of making ground objects, such as man-made objects, water and vegetation, more visible was only analyzed in terms of brightness. We have not only proposed the pseudo-TCT but also designed a series of experiments to verify the image enhancement effects of the pseudo-TCT. We compared the visual effects of different ground objects in different images to determine whether the contrast between the ground objects increased. To examine the separability of typical ground objects from pseudo-TCT images, K-Means and ISODATA clustering were used to examine the separability of buildings and roads from background ground objects [34–37]. Additionally, the spectral characteristics of each typical ground object were visualized by 3D visualization. To verify whether the intra-class coherence and edges of the ground objects were enhanced, the intra-class coherence was visualized by calculating the mean Euclidean distances between the pixel values of each point and the pixel values of eight neighboring points. In addition, we graded the intra-class coherence display to make the effect of edge enhancement clearer and also calculated the standard deviation metric in the NR IQA of the intra-class consistency images. The experimental results showed that the pseudo-TCT can enhance the GF-2 image, increase the separation of typical ground objects and make the edges of typical ground objects clearer. However, we cannot guarantee that pseudo-TCT is useful for some feature extraction algorithms or machine learning methods since we have not verified the effectiveness of pseudo-TCT in practical applications.

2. Materials

2.1. Remote Sensing Data

The base data used in this experiment were two GF-2 images, denoted as image A and image B. Image A was imaged on 19 February 2021, with a fused resolution of 1 m, a longitude of 111.8° E and a latitude of 34.7° N at the center point, and the number of rows and columns being 27,403 × 28,616. Due to the limitation of computer performance, it is not possible to process the whole image, so a part of the area was selected as the data set. To verify the universality of the pseudo-TCT, the selected area required rich types of ground objects, including mountains, lakes, fields, bare soil, rural areas, cities, etc., and a rich variety of building and road styles. The location of each region is shown in Figure 1, which are region 1 (suburban), region 2 (rural with lake), region 3 (mountain) and region 4 (suburban) with the size of 3001 × 3001; region 5 (urban) was the size of 3000 × 3000; mountain 1 (mountain) was the size of 2147 × 2534; and mountain 2 (mountain) was the size of 2629 × 1370.

Image B was from the Gaofen image dataset (GID) [38], a land cover classification datasets produced by Wuhan University, and the images in the GID have been specially processed without latitude and longitude information. It was a GF-2 image, with a resolution of roughly 3–4 m and a dimension of 6800 × 7200 pixels, as shown in the following Figure 2. GID has no resolution information, which was the resolution we infer from the size of the ground objects.

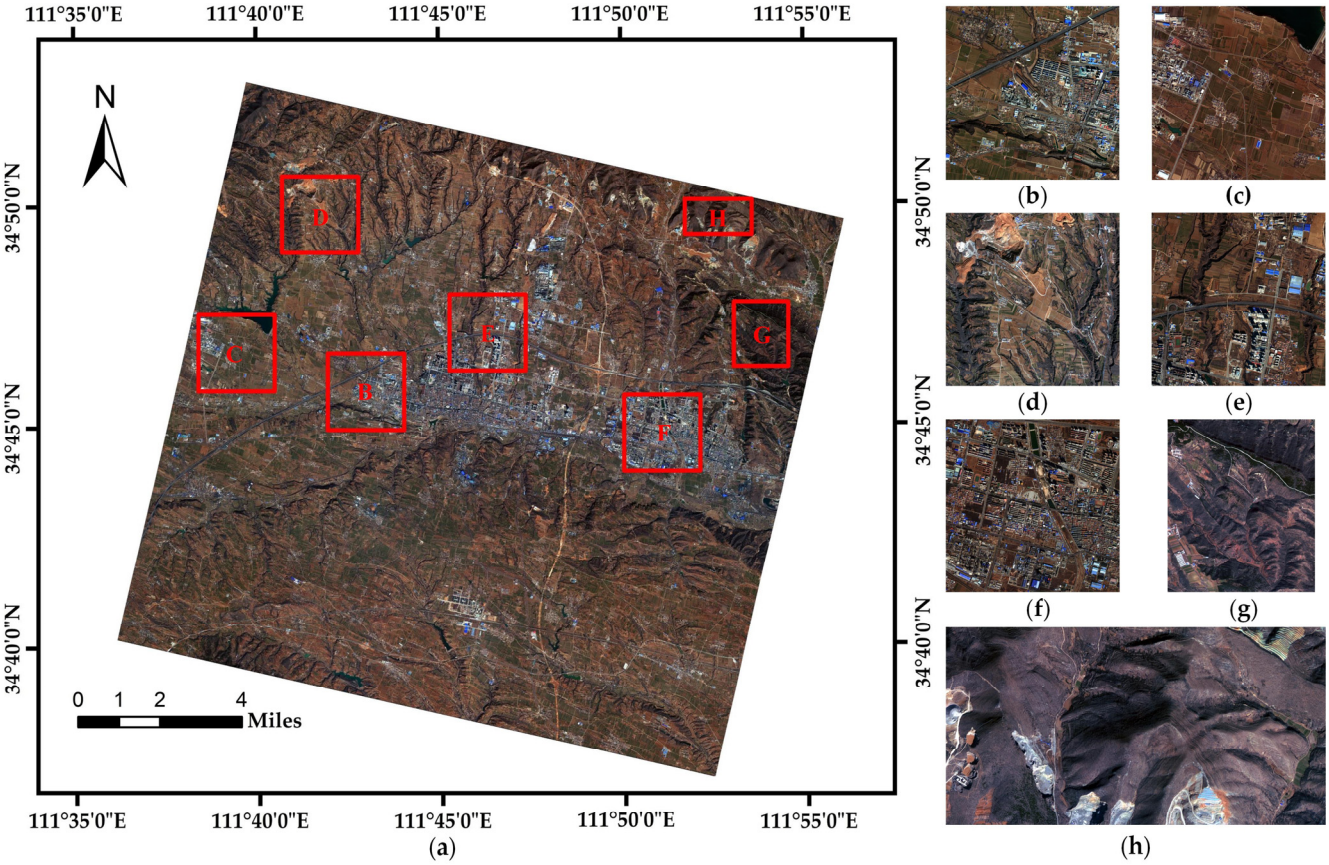

Figure 1. Selected remote sensing data. (**a**) whole GF-2 image; (**b**) region 1, corresponding to B in (**a**); (**c**) region 2, corresponding to C in (**a**); (**d**) region 3, corresponding to D in (**a**); (**e**) region 4, corresponding to E in (**a**); (**f**) region 5, corresponding to F in (**a**); (**g**) mountain 1, corresponding to G in (**a**); (**h**) mountain 2, corresponding to H in (**a**).

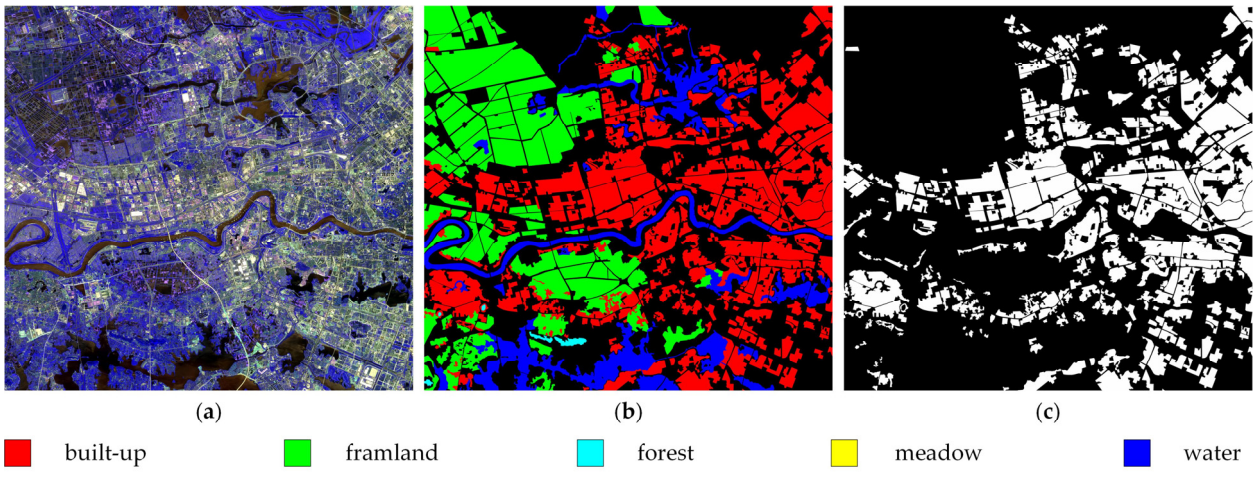

Figure 2. A remote sensing image from GID. (**a**) original image; (**b**) land cover label; (**c**) built-up label.

Image B corresponded to a 5-category land cover classification label, in Figure 2b. Since we evaluate the effect of image enhancement through the clustering effect of buildings and roads, Figure 2c was a label image in which the pixel value of built-up was assigned 1, and the pixels of other categories were assigned 0.

2.2. Data Preprocessing

The objective of atmospheric correction is to determine the true surface reflectance values by removing atmospheric effects from satellite images, while the derivation of the TCT coefficients is generally based on surface reflectance. Although orthorectification and image fusion does not affect the effect of pseudo-TCT, orthorectification can reduce the distortion of remote sensing images and improve the image fusion effect, and image fusion can improve the resolution of images and facilitate the subsequent observation of the details of the enhanced images. Therefore, atmospheric correction, orthorectification and image fusion were performed on image A. It should be noted that when the resolution of multispectral images is 4 times that of panchromatic images, and their resolutions were integers, the effects of image fusion will be better. During orthorectification, the resolutions of multispectral images and panchromatic images would be resampled to 4 m and 1 m, respectively. Image B did not have a panchromatic image, so no image preprocessing was performed.

3. Pseudo-TCT and Verification Experiment

Here, we propose the pseudo-TCT based on the orthogonal linear transform, linear stretching and percentage truncation stretching. The orthogonal linear transformation can obtain new disjoint bands, and the linear stretching and percentage truncation stretching can not only eliminate the negative grey values generated by the orthogonal linear transformation but also further increase the contrast of the remote sensing image and make the effective information of the remote sensing image more concentrated.

Since both buildings and roads were man-made features, we treat buildings and roads as one class. We verify whether the inter-class separability of the enhanced GF-2 images increased by the clustering effects of K-Means clustering and ISODATA clustering on buildings and roads. In addition, we not only directly observed whether the contrast between ground objects of the enhanced remote sensing images increased, but also visualized classical ground objects and intra-class consistency.

3.1. Pseudo-TCT

3.1.1. Orthogonal Linear Transform

The TCT is an empirical orthogonal linear transform of multi-band images proposed by Kauth and Thomas after analyzing the data structure of Landsat MSS images reflecting crop and vegetation growth processes. The TCT relies on the characteristics of the sensor itself, and the TCT coefficients are not universal for different sensors [39]. However, since the parameters of GF-2 and IKONOS were very similar, the TCT coefficients of IKONOS images derived by Horne were directly used as the TCT coefficients of the GF-2 images [40], and the TCT was calculated as follows:

$$u = R^T x + r \quad (1)$$

where u are the bands of the TCT; and R is the TCT coefficients; the superscript T indicates transpose; x is the reflectance of each band; and r is a constant offset to avoid negative values of u after the transformation.

The TCT is a linear combination of different components of different bands, and we want to verify whether there will be better image enhancements if we change the components of these bands, which was the reason why we propose the pseudo-TCT. Since both R and R^T are orthogonal matrices, both can perform an orthogonal linear transformation of the image, so the TCT coefficient matrix without transposition can change the components of different bands and recombine them, so the pseudo-TCT was calculated as follows:

$$u = Rx \quad (2)$$

where u are the bands of the pseudo-TCT; R is the TCT coefficients (same as R in (1)); and x is the reflectance of each band.

3.1.2. Linear Stretching and Percentage Truncation Stretching

After TCT and the pseudo-TCT, there were negative grey values, and the grey values at the two ends of the grey histogram were very small, which reduced the contrast of the image, and the traditional solution is to add a constant offset, r. Since the pseudo-TCT is an orthogonal linear transformation of the GF-2 image, the correlation between the bands is removed, and the stretching can not only remove the negative grey values but also enhance the contrast of the image [18]. Therefore, the linear stretching of the pseudo-TCT image was performed, and the linear stretching was calculated as follows:

$$\text{result} = \frac{(\text{grey} - \min_{\text{in}})}{\max_{\text{in}} - \min_{\text{in}}} \times (\max_{\text{out}} - \min_{\text{out}}) + \min_{\text{out}} \quad (3)$$

where the result is the grey value after stretching; grey is the grey value of the input image; $\min_{\text{in}}$ and $\max_{\text{in}}$ are the minimum and maximum grey values of the input image; and $\min_{\text{out}}$ and $\max_{\text{out}}$ are the minimum and maximum grey values of the output image.

Although linear stretching was performed on the pseudo-TCT image, the contrast of the image was not strong enough and visually dark due to too few values at both ends of the original image grey histogram, so percentage truncation stretching was used to further enhance the image contrast. Percentage truncation stretching is similar to linear stretching in that the grey values are first truncated at the desired scale and then linearly stretched.

3.2. Verification Experiment of Inter-Class Separability

3.2.1. K-Means Clustering and ISODATA Clustering

Unsupervised classification is often used for remote sensing image classification because the acquisition of prior knowledge is tedious. The two commonly used unsupervised classification methods in remote sensing are K-Means clustering and ISODATA clustering, which can divide data with common features into meaningful clusters. This means that ground objects with strong intra-class consistency and high inter-class separability in the image are clustered into one class. Thus, the enhancement effects of the pseudo-TCT can be examined based on the clustering effect on buildings and roads.

The main idea of K-Means is, that given K values and K initial cluster centroids, each point is assigned to the nearest cluster, and then the cluster class centers are recalculated, and then the cluster class centers are assigned and updated in iterations until the class cluster centers are unchanged or the specified number of iterations is reached. Generally, the distance to the cluster center was calculated using the Euclidean distance, which was calculated as follows:

$$D(x, y) = \sqrt{\sum_{i=1}^{n} (x_i - y_i)^2} \quad (4)$$

where $D(x, y)$ is the distance between points x and y; n is the data dimension of x and y; x_i is the value of the i-th dimension of point x; y_i is the value of the i-th dimension of point y.

ISODATA clustering is similar to K-Means clustering, but ISODATA clustering has some improvements compared to K-Means clustering. The ISODATA clustering is based on the K-Means clustering and adds two operations of "merging" and "splitting" to the clustering results, that is, when the value of two cluster centers is less than a certain threshold, the two cluster centers are merged into one, when the standard deviation of a cluster is less than a certain threshold or the number of samples in a cluster exceeds a certain threshold, the cluster is split into two clusters, and even when the number of samples in a cluster is less than a certain threshold, the cluster is cancelled. In addition, ISODATA clustering does not need to set a specific number of categories.

3.2.2. Three-Dimensional Visualization and Intra-Class Consistency Visualization

To observe the spectral features of the pseudo-TCT images and check the separability of ground objects, seven typical ground objects were sampled at the same locations of the original image, TCT image and pseudo-TCT image: bare soil (including uncultivated fields),

buildings, mountains, roads, shadows, vegetation (including cultivated fields) and water bodies. The first three bands of the original image, the TCT image and the pseudo-TCT image were composed into 3D spectral feature space, and the 3D scatter plot of the ground objects was drawn.

The purpose of image enhancement is to increase intra-class consistency and improve separability between classes, making them easier for manual interpretation and machine processing. Compared with similar evaluation metrics, such as cosine similarity, Euclidean distance can take into account the differences in the distance and direction of variables. To verify whether the intra-class consistency of the ground objects of the pseudo-TCT images increased, the Euclidean distance between the pixel values of each point and the pixel values of eight neighboring points, each point with four pixel values, was calculated, and the average of the eight Euclidean distances was used to represent the similarity of the point to the surrounding eight points. This enables the visualization of intra-class consistency, where the grey value of the image is inversely proportional to the intra-class consistency, and a larger grey value indicates a poor intra-class consistency of the ground object. The formula for calculating Euclidean distance is the same as (4), so the formula for calculating the mean value of 8-neighborhood Euclidean distance is as follows:

$$\mathrm{Grey}_x = \frac{\sum_1^8 D(x,\ y_i)}{8} \tag{5}$$

where: Grey_x is the mean Euclidean distance between the grey values of x point and the grey value of the eight neighboring points; $D(x, y_i)$ is the distance between points x and y_i; x is the central point; and y_i is the i-th neighborhood point.

4. Experiments and Results

4.1. Pseudo-TCT of GF-2

From Table 1 it can be seen that the sensor parameters of GF-2 and IKONOS are highly similar, so the TCT coefficients of IKONOS are used directly for GF-2. From the paper "A Tasseled Cap Transformation for IKONOS Images" we know R as follows:

$$R = \begin{bmatrix} 0.326 & -0.311 & -0.612 & -0.650 \\ 0.509 & -0.356 & -0.312 & 0.719 \\ 0.560 & -0.325 & 0.722 & -0.243 \\ 0.567 & 0.819 & -0.081 & -0.031 \end{bmatrix} \tag{6}$$

Table 1. Main parameters of GF-2 and IKONOS.

Main Parameters	Spectra	GF-2	IKONOS
Type of orbit		Regression Sun-synchronous orbit	Sun-synchronous orbit
Orbit height		631 km	681 km
Orbital inclination		97.9080°	98.1°
Spectral range	Panchromatic	0.45–0.90 μm	0.45–0.90 μm
	Multispectral	0.45–0.52 μm	0.45–0.53 μm
		0.52–0.59 μm	0.52–0.61 μm
		0.63–0.69 μm	0.64–0.72 μm
		0.77–0.89 μm	0.77–0.88 μm
Spatial resolution	Panchromatic	0.8 m (1 m after orthorectification)	1 m
	Multispectral	3.2 m (4 m after orthorectification)	4 m

To avoid negative grey values after pseudo-TCT, each band of the pseudo-TCT image was linearly stretched to [0, 65,535], since the GF-2 image is a 16-bit image. Since the original image has fewer values at the ends of the grey histogram, the overall image perception is still dark after linear stretching. Therefore, the image was then stretched with a percentage truncation, with a minimum and maximum exclusion ratio of 10% and a stretching range

of [0, 255]. The grey value corresponding to 10% and the grey value corresponding to 90% of each band were calculated, and the two values were regarded as the minimum and maximum of the grey values of the corresponding band, and the grey values located between 10% and 90% was linearly stretched to [0, 255], and the grey values smaller than the minimum was directly assigned to 0, and the grey values larger than the maximum was assigned to 255.

Since each band of the pseudo-TCT image no longer has the physical meaning of each band of the TCT image, it is not necessary to calculate the pseudo-TCT according to the original band order of the TCT, and the four bands can be arranged and combined to obtain 24 pseudo-TCT combinations. For the convenience of description, the blue band is 0, the green band is 1, the red band is 2 and the NIR band is 3. For example, the 0123 combination is as follows:

$$u_1 = 0.326x_0 - 0.311x_1 - 0.612x_2 - 0.650x_3 \quad (7)$$

$$u_2 = 0.509x_0 - 0.356x_1 - 0.312x_2 + 0.719x_3 \quad (8)$$

$$u_3 = 0.560x_0 - 0.325x_1 + 0.722x_2 - 0.243x_3 \quad (9)$$

$$u_4 = 0.567x_0 + 0.819x_1 - 0.081x_2 - 0.031x_3 \quad (10)$$

where u_1, u_2, u_3 and u_4 denote the bands of the pseudo-TCT, and x_0, x_1, x_2 and x_3 denote the blue band, green band, red band and near-infrared band, respectively.

Region 2, region 3 and region 4, which are rich in types of ground objects and relatively representative, were selected to demonstrate the visual effect of the pseudo-TCT. The original images, TCT images and a portion of the corresponding pseudo-TCT images are shown in Figure 3.

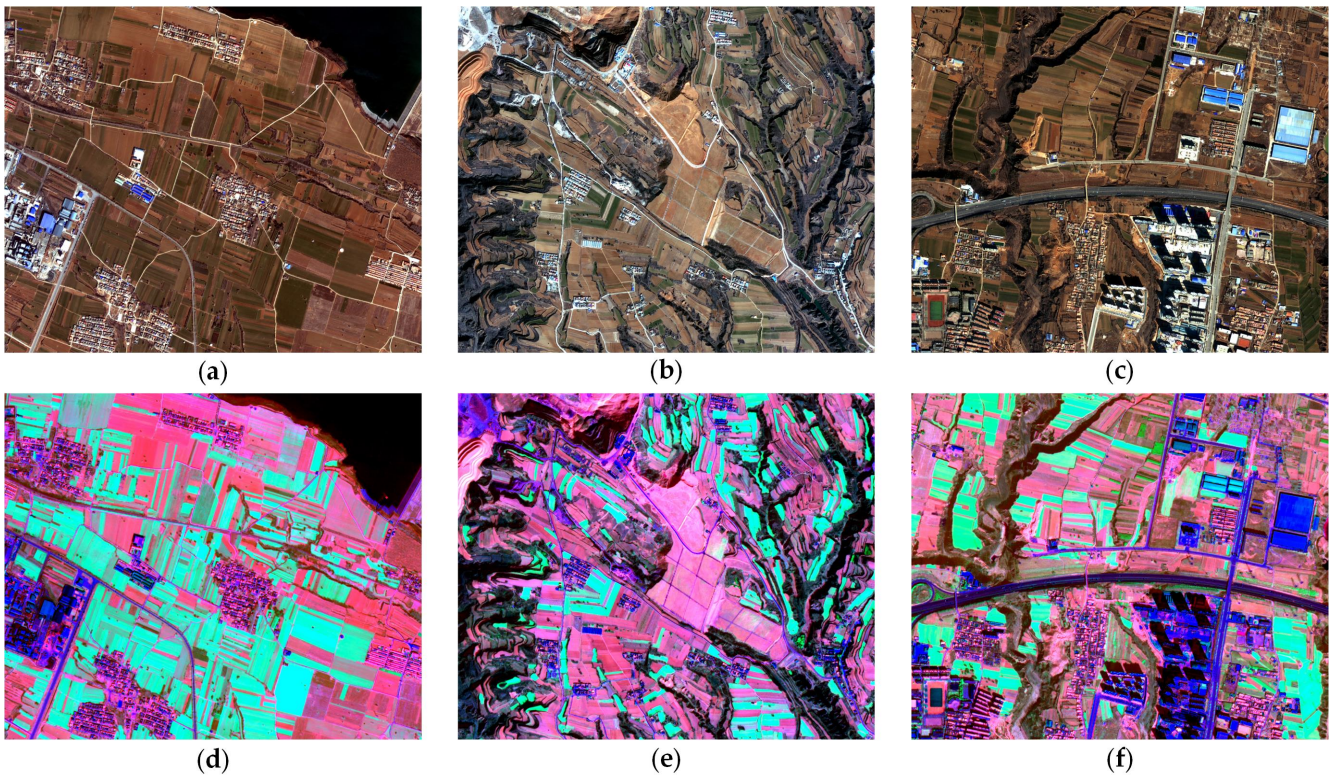

Figure 3. *Cont.*

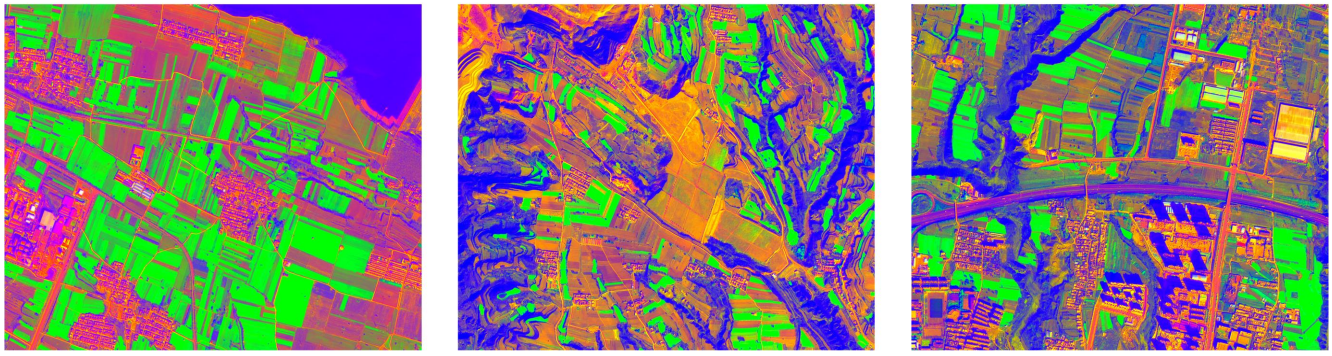

(**g**) (**h**) (**i**)

Figure 3. Original images, TCT images, and 0123 combination images of region 2, region 3, and region 4. (**a**) original image of region 2; (**b**) original image of region 3; (**c**) original image of region 4; (**d**) TCT image of region 2; (**e**) TCT image of region 3; (**f**) TCT image of region 4; (**g**) 0123 combination image of region 2; (**h**) 0123 combination image of region 3; (**i**) 0123 combination image of region 4.

It can be seen from Figure 3 that the visual effect of the images is improved in both the 0123 combination images and the TCT images relative to the original images. It can also be seen from Figure 3 that shadows and water bodies are relatively similar in the images, which is consistent with other image segmentation studies that shadows and water bodies are easily confused. In addition, buildings and roads are enhanced in both the TCT images and the 0123 combination images.

4.2. High Precision Label Making

The separability check of the pseudo-TCT image requires a high-precision label of buildings and roads, and traditional labeling is usually performed manually. Manual labeling can easily miss small buildings and roads, or buildings and roads are labeled with background information, which can lead to inaccurate accuracy evaluation results [41–44].

To solve the problem whereby it is difficult to produce a large high-precision label by traditional methods, a combination of pseudo-TCT images, such as the 0123 combination, was selected and clustered into 10 classes using K-Means. The classes containing buildings and roads in the K-Means classification were converted to vector files and then further edited in ArcGIS to obtain the label. The label was manually edited to eliminate the effect of the 0123 combination. The K-Means clustering results and vector labels for region 2, region 3 and region 4 (containing more than 99% of buildings and roads) are shown in Figure 4.

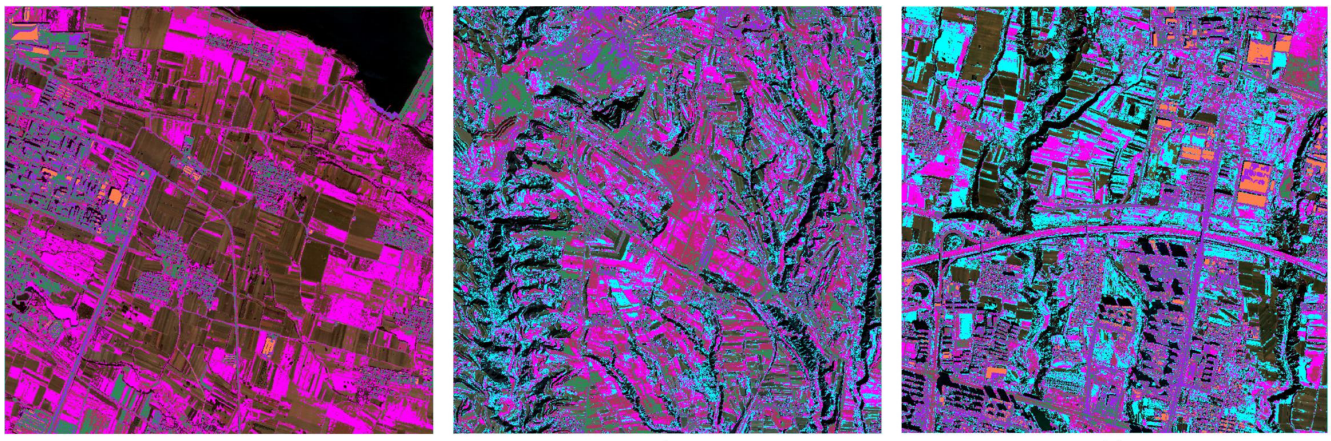

(**a**) (**b**) (**c**)

Figure 4. *Cont.*

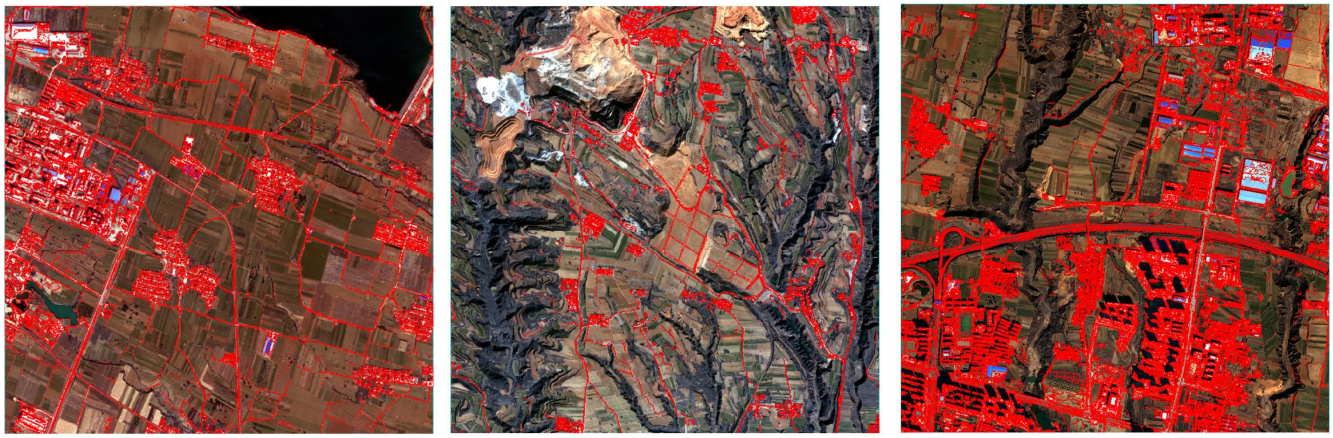

(d) (e) (f)

Figure 4. K-Means clustering results and vector labels for region 2, region 3, and region 4. (**a**) region 2 K-Means clustering result; (**b**) region 3 K-Means clustering result (**c**) region 4 K-Means clustering result (**d**) region 2 vector label (**e**) region 3 vector label; (**f**) region 4 vector label.

4.3. Inter-Class Separability and Intra-Class Consistency Validation Experiments

4.3.1. K-Means Clustering and ISODATA Clustering Test for Inter-Class Separability

Region 2, region 3, region 4 and image B were selected as the regions to test the inter-class separability of the pseudo-TCT images. K-Means clustering was used for region 2, region 3 and region 4, and ISODATA clustering was used for region 4 and image B. The clustering effect is the best when the number of cluster centers K is generally slightly larger than the number of categories, so in this experiment, the K-Means were clustered into 10 categories and the number of iterations was set to 1. The categories in the clustering results were selected until the selected categories contained more than 99% of buildings and roads. The evaluation of clustering effects is usually performed with internal evaluation and external evaluation. Internal evaluation is usually used to evaluate the impacts of different algorithms or different ways of running algorithms on the clustering results based on the same raw data and is highly biased toward certain types of clustering models [45]. External evaluation requires knowing the category to which each pixel point belongs, which is very difficult in remote sensing image classification. Therefore, they cannot be used to evaluate the clustering results of this experiment. Since there are labels for buildings and roads, then the evaluation metrics commonly used in classification can be used to evaluate the clustering effects of buildings and roads. A better evaluation result can only indicate that the selected categories contain more buildings and roads and fewer background ground objects. The accuracy of the buildings and roads extracted by K-Means was evaluated using Accuracy, Precision, Recall, F1-score, IoU, Kappa, Recall of buildings and roads (1_Recall) and the number of categories. The image with the highest F1-score and the lowest number of selected categories is the one with the best separation of buildings and roads from the background ground objects. The evaluation metrics were defined as follows:

$$\text{Accuracy} = \frac{\text{TP} + \text{TN}}{\text{TP} + \text{FN} + \text{FP} + \text{TN}} \tag{11}$$

$$\text{Precision} = \frac{\text{TP}}{\text{TP} + \text{FP}} \tag{12}$$

$$\text{Recall} = \frac{\text{TP}}{\text{TP} + \text{FN}} \tag{13}$$

$$\text{F1} = \frac{2 \times \text{TP}}{2 \times \text{TP} + \text{FP} + \text{FN}} \tag{14}$$

$$\text{IoU} = \frac{\text{Precision} \times \text{Recall}}{\text{Precision} + \text{Recall} - \text{Precision} \times \text{Recall}} \tag{15}$$

$$\text{Kappa} = \frac{p_0 - p_e}{1 - p_e} \tag{16}$$

$$1\_\text{Recall} = \frac{1\_\text{TP}}{1\_\text{TP} + 1\_\text{FN}} \tag{17}$$

In the classification, true positives (TPs) and true negatives (TNs) denote the number of building and road pixels identified correctly and the number of background ground object pixels identified correctly, respectively, whereas false positives (FPs) and false negatives (FNs) denote the number of building and road pixels identified incorrectly and the number of background ground object pixels identified incorrectly, respectively. All evaluation metrics are calculated by macro-averaging, which calculates the corresponding evaluation metric for each category, and then averages the results together, so 1_Recall denotes the Recall of buildings and roads. The p_0 in Kappa is the same as Accuracy and p_e is the sum of the product of the actual number of each class and the predicted number of each class divided by the square of the total number of samples. The range of Kappa is $[-1, 1]$. If Kappa is positive, a greater kappa indicates a higher classification accuracy; if Kappa is negative, it indicates a particularly poor classification accuracy.

The classification evaluation results of the original images, the TCT images and the pseudo-TCT images of each combination of region 2, region 3 and region 4 are shown in Table A1. To show the differences between the images with the best evaluation result and the rest of the images, we selected the second-best, medium and worst pseudo-TCT combination images for the evaluation result, as shown in Figure 5. There were 24 combination images, so only region 2 was selected to be shown in Figure A1 to further demonstrate the differences in the different combination images.

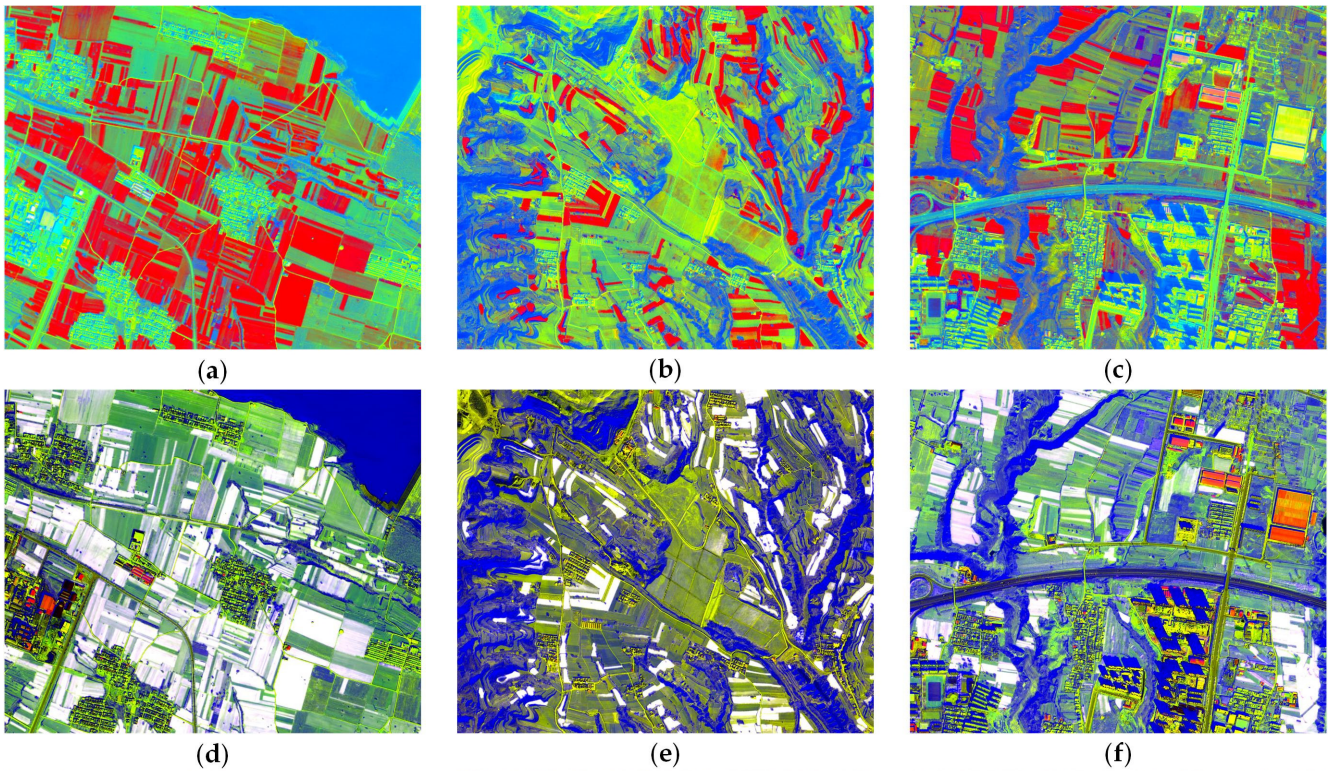

Figure 5. *Cont.*

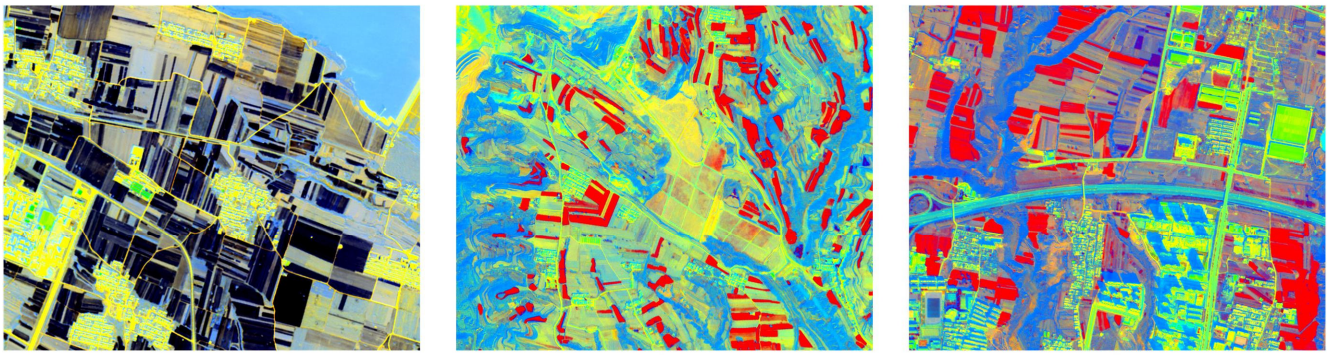

(**g**) (**h**) (**i**)

Figure 5. Other combination images of region 2, region 3, and region 4. The combination images with the second best, medium, and worst evaluation result accuracy are indicated from top to bottom, respectively. (**a**) 0132 combination image of region 2; (**b**) 0132 combination image of region 3; (**c**) 0132 combination image of region 4; (**d**) 3102 combination image of region 2; (**e**) 3201 combination image of region 3; (**f**) 3102 combination image of region 4; (**g**) 2310 combination image of region 2; (**h**) 2130 combination image of region 3; (**i**) 2130 combination image of region 4.

Although these images do not have the best evaluation result, they all have improved visualization compared to the original images. Vegetation, buildings and roads are more prominent in these images.

Because the 0123-combination image had the best clustering effect in K-Menas, so regardless of other combinations, only the 0123-combination image of region 4 and image B were selected for ISODATA clustering. The ground objects in remote sensing images can be roughly divided into seven categories, which are bare soil, buildings, mountains, roads, shadows, vegetation and water bodies, so the classification number of ISODATA clustering is set from 4 to 10. The remaining parameters only need to ensure that the 0123 combination of region 4 is the same as that of image B, the number of iterations is set to five, the change threshold is set to 5%, the minimum number of pixels in each category is set to one and the maximum standard deviation of each category is set to one, and the maximum value of merged classes is set to two. If the main part of a category is buildings and roads, it is selected as the result of clustering. The clustering results are shown in Figure 6.

The accuracy of ISODATA clustering results was evaluated using the same metrics as K-Means clustering, and the results were shown in Table 2.

Table 2. Evaluation of ISODATA clustering.

Image	Accuracy	Precision	Recall	F1	IoU	Kappa	1_Recall
Region4							
0123	0.9184	0.9124	0.8665	0.8862	0.8010	0.7729	0.7612
Original	0.8435	0.8593	0.7115	0.7466	0.6210	0.5058	0.4434
TCT	0.8822	0.8729	0.8029	0.8293	0.7197	0.6607	0.6420
Image B							
0123	0.7237	0.6659	0.6885	0.6728	0.5213	0.3491	0.6122
Original	0.7492	0.6739	0.6485	0.6574	0.5161	0.3177	0.4306
TCT	0.7535	0.6818	0.6647	0.6716	0.5289	0.3444	0.4729

4.3.2. 3D Visualization of Typical Ground Objects and Visualization of Intra-Class Consistency

Table A1 shows that the 0123-combination image has the best separability of buildings and roads from background ground objects relative to the original image and the TCT image. To analyze the spectral features of the original image, TCT image and 0123-combination image, seven typical ground objects, which are bare soil, buildings, mountains, roads, shadows, vegetation, and water bodies, were selected in region 1, region 2, region 3, region

5, mountain 1 and mountain 2, respectively. The sampling point locations of the three images are identical, and the duplicate values are excluded, and the results are as follows in Table 3. The 0123-combination image has the least number of sampling points, which also indicates that the 0123-combination image has the best intra-class consistency. The first three components of the original image, the TCT image (the TCT image was also linearly stretched, and percentage truncated to ensure a fair comparison with the pseudo-TCT) and the 0123-combination image were linearly stretched to 0–255 and then mapped to the 3D space, and the results are shown in Figure 7.

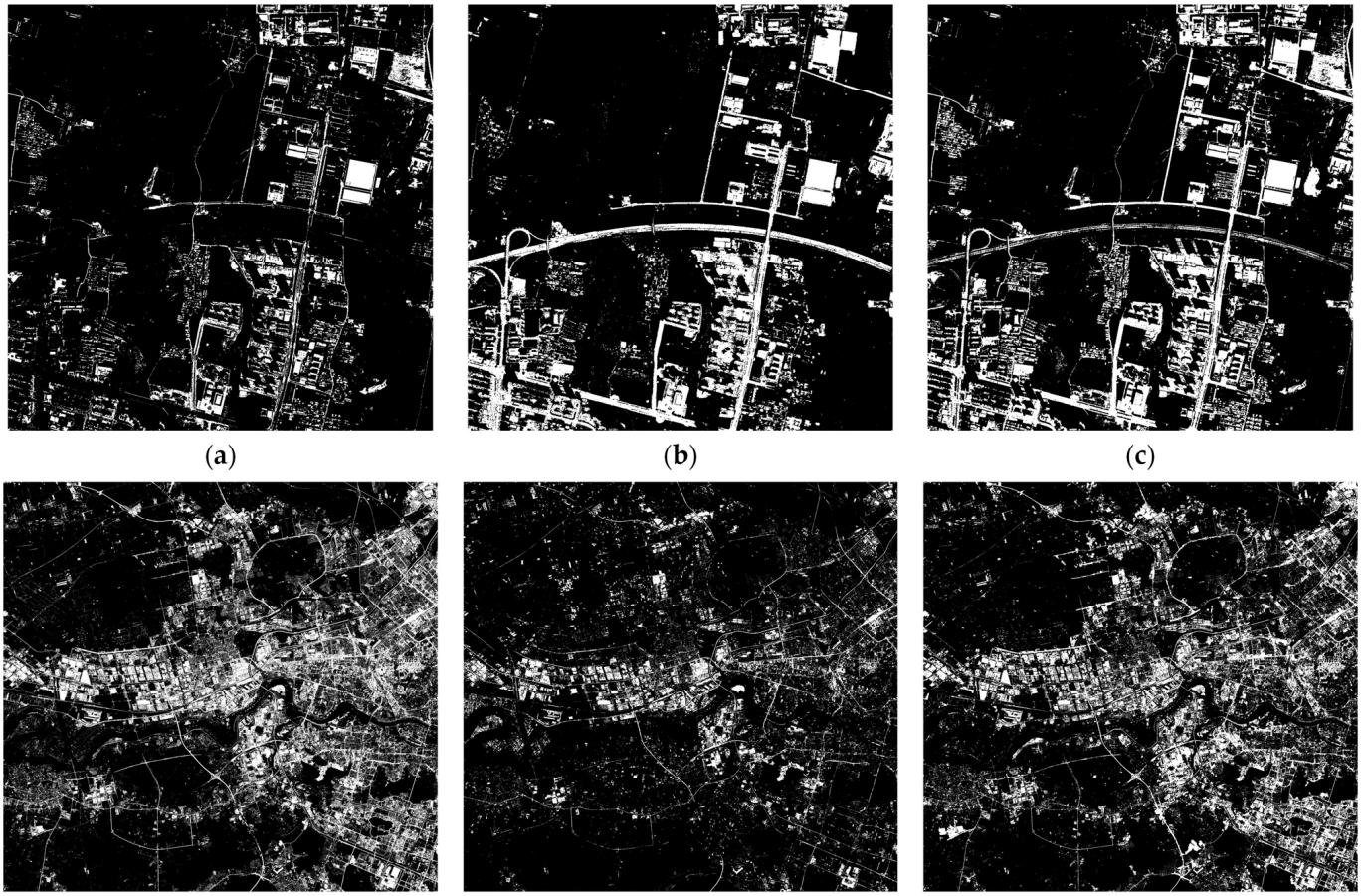

Figure 6. ISODATA clustering results. (**a**) region 4 clustering result of the original image; (**b**) region 4 clustering result of TCT image; (**c**) region 4 clustering result of 0123 combination image; (**d**) image B clustering result of the original image; (**e**) image B clustering result of TCT image; (**f**) image B clustering result of 0123 combination image.

Table 3. Typical ground objects sampling points.

Image	Bare Soil	Building	Mountain	Road	Shadow	Vegetation	Water Body	Total
Original	48,190	18,010	24,169	12,394	8850	22,475	76,827	210,915
TCT	35,365	7389	20,578	9435	2767	14,302	175	90,011
0123	37,708	7368	18,388	7304	919	10,828	2648	85,163

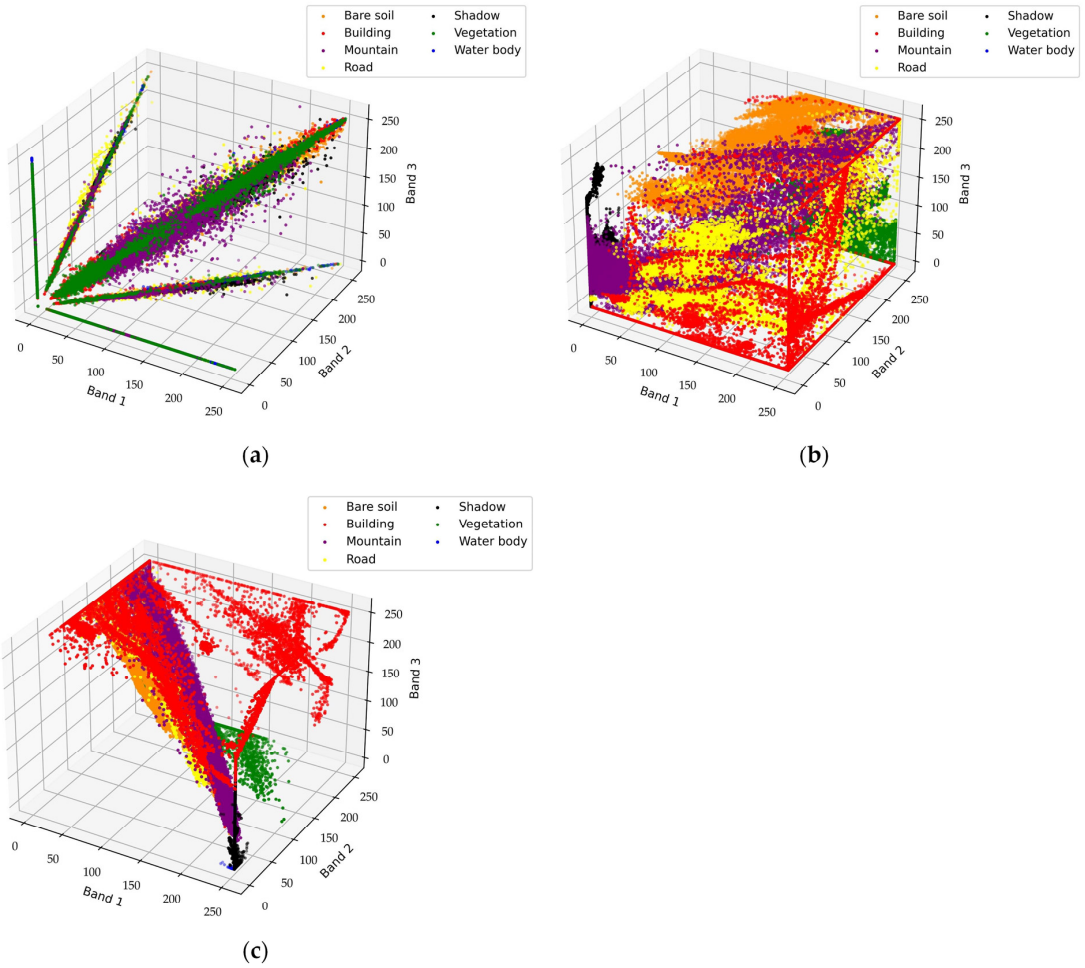

Figure 7. 3D scatter plot of typical ground objects. The dark orange dots, red dots, purple dots, yellow dots, black dots, green dots, and blue dots indicate the bare soil, buildings, mountains, roads, shadows, vegetation and water bodies, respectively. (**a**) 3D scatter plot of the original image; (**b**) 3D scatter plot of the TCT image; (**c**) 3D scatter plot of the 0123-combination image.

To observe the intra-class consistency more visually and analyze whether the intra-class consistency of the 0123-combination image is enhanced, the intra-class consistency of the original image, the TCT image and the pseudo-TCT image in region 4 were visualized hierarchically, and the results are shown in Figures 8 and 9.

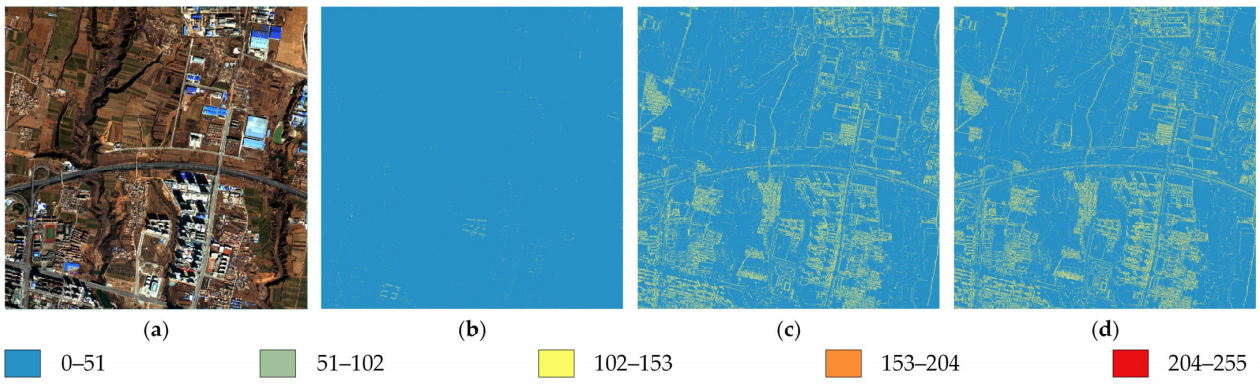

Figure 8. Intra-class consistency image. (**a**) original image; (**b**) intra-class consistency image of the original image; (**c**) intra-class consistency image of the TCT image; (**d**) intra-class consistency image of 0123 combination image.

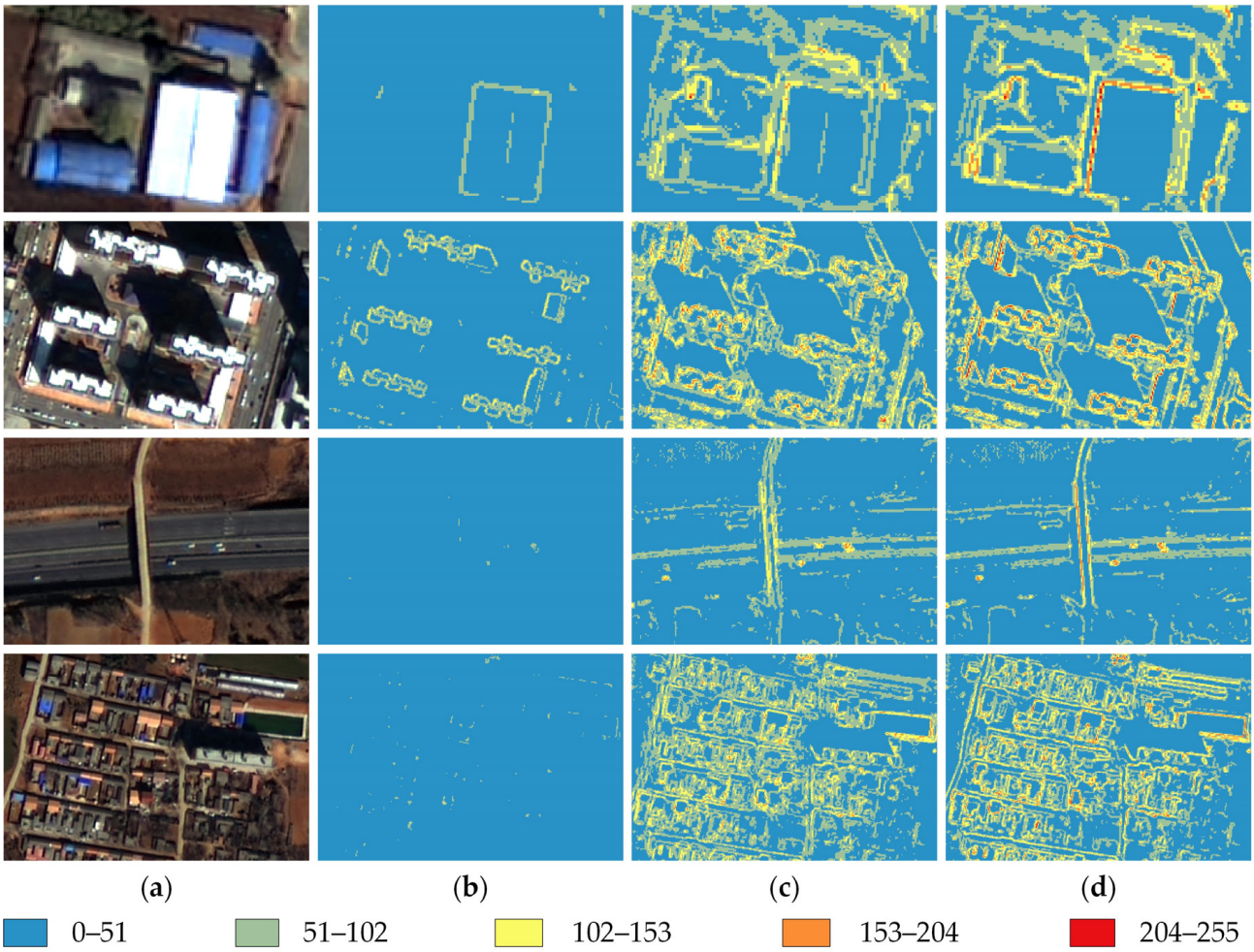

Figure 9. Local images of intra-class consistency of different images. (**a**) local images of the original image; (**b**) local images of intra-class consistency image of the original image; (**c**) local images of intra-class consistency image of the TCT image; (**d**) local images of intra-class consistency image of the pseudo-TCT image.

To quantify the effect of image enhancement, we calculated the standard deviations of the intra-class consistency image of the original image, the intra-class consistency image of the TCT image, and the intra-class consistency image of the pseudo-TCT image, which were 8.93, 26.74, and 30.15, respectively.

5. Discussion

5.1. Visual Effect Comparison

From Figure 3, it can be seen that the contours of typical ground objects are enhanced, intra-class consistency is significantly enhanced and minor textures are eliminated in the pseudo-TCT image compared with the original image. Compared with the TCT image, not only is the contrast of the ground objects further improved but also the contours of the ground objects are clearer. Furthermore, the pseudo-TCT images are displayed in a more realistic pseudo-color. Vegetation is shown in green, shadows and water bodies in blue, buildings and roads in purple and orange, and bare soil in brown. Vegetation growth and water transparency can be indicated by the color shades, which is more beneficial to manual interpretation. From Figures 5 and A1, it can be found that different combinations of the pseudo-TCT images can enhance the visual effects of ground objects, and all images make buildings, roads, and vegetation more prominent. However, it is impossible to find out which combination image has the best effect from the images only because some

combination images have similar visual effects. With the continuous development of big data and machine learning, remote sensing images also need more and more labeled data, and the enhancement of visual effects is important to produce labeled data. Unfortunately, due to the limited data in this experiment, it is impossible to verify whether the visual effects on other images will be also enhanced by the pseudo-TCT.

5.2. Comparison of K-Means Clustering Results and ISODATA Clustering Results

The evaluation of the clustering results for buildings and roads can indicate how many buildings and roads are included in the clustering results. From Table A1, we can find that the 0123 combination only needs 7~8 categories to include more than 99% of buildings and roads, and each evaluation metric is the best (1_Recall is the coverage rate of buildings and roads). In region 2, the accuracy of the 0123-combination image is 53.82% higher than the accuracy of the original image and the TCT image. The difference of each evaluation metric between the 0123 and 0132 combinations is within 0.05, which indicates that buildings and roads have similar spectral characteristics in the red band and NIR band. This is consistent with the spectral characteristics of buildings and roads in the principles of using red light bands to distinguish artificial ground objects and grasslands and using near-infrared and infrared bands to construct a building index (NDBI). In region 4, although the 1230, 1203, 1023, 0231 and 0213 combinations contain all buildings and roads with only 8–9 categories, there are too many background ground objects interspersed, so the separability of buildings and roads from the background ground objects is not as good as the 0123 combination.

As shown in Table 2, the 0123-combination images of region 4 and image B have the highest F1-score and Kappa, and it can also be seen from Figure 6 that the buildings and roads extracted from the 0123-combination images are more complete and clearer. The clustering results, although none of them are very good, can show that the pseudo-TCT makes it easier to distinguish buildings and roads from other ground objects. Although K-Means clustering and ISODATA clustering evaluated the separability of buildings and roads from background ground objects, there are still some ground objects where the separability needs to be verified. The clustering of buildings and roads is only used to select the best pseudo-TCT combination and to compare the intra-class consistency of the pseudo-TCT images, the original images and the TCT images, and is not used to extract buildings and roads. Only using pseudo-TCT and clustering cannot extract buildings and roads well; if we want to obtain better extraction results, we need to combine other methods.

5.3. Spectral Feature Visualization and Intra-Class Consistency Analysis

From Figure 7a, it can be found that the various ground objects of the original image are completely mixed together and completely dispersed in the 3D space. From Figure 7b, it can be found that the various ground objects in the TCT image are separated compared with the original image, but the mountains, roads, bare soil and buildings are interspersed and not concentrated enough. From Figure 7c, there is a slight overlap of bare soil, roads and buildings in the 0123-combination image and the water bodies and shadows are closer together. The ground objects are not only separated but also relatively concentrated and unified in direction. Bare soil, shadows, water bodies, mountains, roads and vegetation are more concentrated, indicating that the intra-class consistency of these six ground objects was enhanced after pseudo-TCT processing. Overall, it seems that the ground objects in the 0123-combined image are most concentrated in the spectral feature space, with the best separability of the ground objects and more uniformity in direction.

Table 3 shows that the typical ground objects in the 0123-combined image have the least number of sampling points, with only 40.38% of the original image and 94.61% of the TCT image. Figures 8 and 9 show that the interior of the buildings and roads in the 0123-combined image are more consistent and the edges of the buildings and roads are more clearly defined. The standard deviation of the intra-class consistency images for the 0123-combination image of region 4 and image B is the highest at 30.15, which is approximately three times that of the original image. A larger standard deviation indicates

a higher image contrast and sharper edges. All of these points show that the pseudo-TCT can enhance the intra-class consistency of the images and make the edges of the ground objects clearer. Although the edges of the ground objects are sharper and the intra-class consistency within the ground objects is higher, it is not possible to determine whether these features are more conducive to deep learning or feature extraction algorithms and whether these features can be learned as we have not tested them using deep learning or feature extraction algorithms.

6. Conclusions

In this study, we proposed the pseudo-TCT by using the orthogonal linear transformation idea in the TCT and further enhanced the image enhancement effects by using linear stretching and percentage truncation stretching. K-Means clustering and ISODATA clustering were used to examine the separability of buildings and roads from background ground objects. The visualization method was used to visualize the spectral characteristics and intra-class consistency of typical ground objects and we calculated the standard deviation of the intra-class consistency maps.

The results of the validation experiments show that the pseudo-TCT can significantly enhance the GF-2 images, not only improving the visual interpretation but also improving the separability and edges of ground objects. Buildings and roads, as man-made ground objects, have similar spectral characteristics, so they can be considered as one category. Because of the increased separability of buildings and roads from the rest of the ground objects, it is easier for buildings and roads to be clustered together and not confused with other ground objects. At least in the unsupervised classification of extracted buildings and roads, the pseudo-TCT images performed better than the original and TCT images. However, we did not verify the effectiveness of the pseudo-TCT in feature extraction algorithms or machine learning methods, nor did we compare it with traditional remote sensing image enhancement methods, such as NDWI, NDBI, NDVI, etc., because the practical applications are very complicated. In the future, we will use additional images and other ground objects to validate pseudo-TCT and more deep learning and feature extraction algorithms to test whether pseudo-TCT is useful for these methods, and also to verify under which applications the pseudo-TCT will work better.

Author Contributions: Conceptualization, J.D.; data curation, W.D., Y.G., X.C. and R.Z.; formal analysis, J.D.; funding acquisition, W.L.; investigation, J.D.; methodology, W.D.; project administration, J.D.; resources, W.L.; software, W.D.; supervision, J.D.; validation, W.D.; visualization, W.D.; writing—original draft, W.D.; writing—review and editing, J.D. and W.D. All authors have read and agreed to the published version of the manuscript.

Funding: This research was funded by National Natural Science Foundation of China (Grant Number: 42172330) and 2021 Henan Natural Resources Research Project (Grant Number: [2021]157-12).

Institutional Review Board Statement: Not applicable.

Informed Consent Statement: Not applicable.

Data Availability Statement: Not applicable.

Acknowledgments: The authors would like to thank the editors and reviewers for their valuable suggestions.

Conflicts of Interest: The authors declare no conflict of interest.

Appendix A

Table A1. Evaluation of K-Means clustering.

Image	Accuracy	Precision	Recall	F1	IoU	Kappa	1_Recall	Class Number
Region 2								
3210	0.3679	0.6028	0.6186	0.3672	0.2251	0.0948	0.9958	9
3201	0.3670	0.6026	0.6180	0.3663	0.2244	0.0942	0.9956	9
3120	0.3636	0.6025	0.6163	0.3630	0.2219	0.0925	0.9965	9
3102	0.3602	0.6021	0.6144	0.3598	0.2195	0.0907	0.9966	9
3021	0.3579	0.6019	0.6130	0.3576	0.2178	0.0894	0.9967	9
3012	0.3555	0.6017	0.6116	0.3552	0.2160	0.0881	0.9970	9
2310	0.2048	0.5869	0.5223	0.1910	0.1094	0.0154	0.9999	9
2301	0.3259	0.5980	0.5940	0.3258	0.1946	0.0722	0.9973	8
2130	0.2853	0.5942	0.5703	0.2835	0.1657	0.0520	0.9990	9
2103	0.4469	0.6121	0.6631	0.4394	0.2838	0.1413	0.9883	8
2031	0.2796	0.5933	0.5667	0.2774	0.1616	0.0492	0.9987	9
2013	0.2327	0.5883	0.5387	0.2246	0.1287	0.0274	0.9990	9
1320	0.3461	0.6017	0.6070	0.3461	0.2093	0.0837	0.9995	8
1302	0.3646	0.6038	0.6178	0.3640	0.2227	0.0938	0.9989	8
1230	0.2934	0.5957	0.5755	0.2921	0.1714	0.0563	0.9998	8
1203	0.2856	0.5948	0.5708	0.2839	0.1659	0.0524	0.9997	8
1032	0.4978	0.6246	0.6977	0.4841	0.3234	0.1801	0.9983	8
1023	0.3301	0.5998	0.5974	0.3301	0.1977	0.0751	0.9996	9
0321	0.3556	0.6030	0.6128	0.3553	0.2161	0.0890	0.9996	8
0312	0.3729	0.6052	0.6231	0.3720	0.2287	0.0987	0.9995	8
0231	0.6343	0.6559	0.7782	0.5979	0.4371	0.2980	0.9947	7
0213	0.6705	0.6673	0.7997	0.6282	0.4702	0.3367	0.9940	7
0132	0.6622	0.6649	0.7954	0.6214	0.4626	0.3280	0.9958	7
0123	0.7058	0.6798	0.8200	0.6582	0.5041	0.3778	0.9919	7
Original	0.1676	-	0.5000	-	0.0838	0.0000	1.0000	10
TCT	0.1676	-	0.5000	-	0.0838	0.0000	1.0000	10
Region 3								
3210	0.1643	0.5266	0.5577	0.1607	0.0884	0.0128	0.9943	9
3201	0.1632	0.5267	0.5572	0.1597	0.0877	0.0127	0.9946	9
3120	0.1599	0.5266	0.5557	0.1567	0.0859	0.0123	0.9951	9
3102	0.1569	0.5267	0.5545	0.1541	0.0842	0.0120	0.9959	9
3021	0.1544	0.5268	0.5536	0.1518	0.0828	0.0118	0.9966	9
3012	0.1527	0.5268	0.5528	0.1502	0.0819	0.0116	0.9970	9
2310	0.1611	0.5271	0.5572	0.1579	0.0866	0.0127	0.9969	8
2301	0.1629	0.5273	0.5583	0.1595	0.0876	0.0129	0.9971	8
2130	0.1151	0.5261	0.5339	0.1148	0.0610	0.0072	0.9989	8
2103	0.3196	0.5336	0.6408	0.2848	0.1760	0.0375	0.9974	7
2031	0.1589	0.5277	0.5573	0.1558	0.0853	0.0127	0.9996	8
2013	0.3316	0.5339	0.6458	0.2932	0.1828	0.0395	0.9947	8
1320	0.1523	0.5275	0.5539	0.1499	0.0817	0.0118	0.9997	8
1302	0.1639	0.5279	0.5599	0.1603	0.0881	0.0133	0.9996	8
1230	0.1251	0.5267	0.5396	0.1245	0.0665	0.0085	0.9998	8
1203	0.1253	0.5266	0.5396	0.1247	0.0667	0.0085	0.9995	8
1032	0.2435	0.5307	0.6018	0.2274	0.1328	0.0247	0.9997	8
1023	0.2457	0.5307	0.6029	0.2292	0.1340	0.0251	0.9994	8
0321	0.2092	0.5289	0.5824	0.1994	0.1134	0.0193	0.9966	7
0312	0.2222	0.5293	0.5889	0.2101	0.1207	0.0211	0.9959	6
0231	0.1720	0.5281	0.5641	0.1676	0.0927	0.0144	0.9994	7
0213	0.1263	0.5268	0.5403	0.1256	0.0672	0.0086	0.9999	8
0132	0.3723	0.5361	0.6676	0.3215	0.2063	0.0479	0.9955	7
0123	0.3823	0.5370	0.6744	0.3284	0.2121	0.0505	0.9986	7
Original	0.0496	-	0.5000	-	0.0248	0.0000	1.0000	10
TCT	0.0496	-	0.5000	-	0.0248	0.0000	1.0000	10

Table A1. *Cont.*

Image	Accuracy	Precision	Recall	F1	IoU	Kappa	1_Recall	Class Number
Region 4								
3210	0.3609	0.6314	0.5689	0.3477	0.2143	0.0755	0.9911	9
3201	0.3605	0.6312	0.5686	0.3473	0.2140	0.0751	0.9910	9
3120	0.3588	0.6330	0.5681	0.3451	0.2125	0.0744	0.9928	9
3102	0.3575	0.6332	0.5673	0.3434	0.2114	0.0735	0.9933	9
3021	0.3560	0.6334	0.5664	0.3415	0.2101	0.0725	0.9937	9
3012	0.3550	0.6336	0.5659	0.3403	0.2093	0.0719	0.9941	9
2310	0.3363	0.6350	0.5547	0.3166	0.1938	0.0587	0.9979	9
2301	0.3332	0.6305	0.5518	0.3129	0.1913	0.0555	0.9955	9
2130	0.3011	0.6323	0.5316	0.2701	0.1649	0.0331	0.9997	9
2103	0.4648	0.6560	0.6390	0.4640	0.3023	0.1643	0.9925	8
2031	0.3072	0.6324	0.5356	0.2784	0.1699	0.0375	0.9993	9
2013	0.3280	0.6359	0.5495	0.3057	0.1868	0.0529	0.9994	9
1320	0.3578	0.6411	0.5696	0.3431	0.2113	0.0758	0.9996	8
1302	0.3629	0.6418	0.5730	0.3493	0.2155	0.0798	0.9995	8
1230	0.3247	0.6365	0.5475	0.3013	0.1841	0.0506	1.0000	8
1203	0.3077	0.6340	0.5361	0.2789	0.1702	0.0380	1.0000	8
1032	0.4121	0.6507	0.6061	0.4067	0.2569	0.1203	0.9999	9
1023	0.4225	0.6526	0.6131	0.4183	0.2657	0.1292	1.0000	9
0321	0.3672	0.6418	0.5757	0.3546	0.2192	0.0831	0.9989	8
0312	0.3716	0.6425	0.5786	0.3599	0.2229	0.0865	0.9988	8
0231	0.3210	0.6360	0.5451	0.2966	0.1811	0.0479	1.0000	8
0213	0.3032	0.6335	0.5331	0.2729	0.1666	0.0348	1.0000	8
0132	0.5635	0.6838	0.7075	0.5621	0.3913	0.2647	0.9999	7
0123	0.5911	0.6914	0.7260	0.5882	0.4175	0.2951	0.9998	8
Original	0.2537	-	0.5000	-	0.1269	0.0000	1.0000	10
TCT	0.2550	0.4570	0.4991	0.2054	0.1283	-0.0009	0.9947	9

"-" means no value. This value cannot be calculated because the denominator is 0.

Appendix B

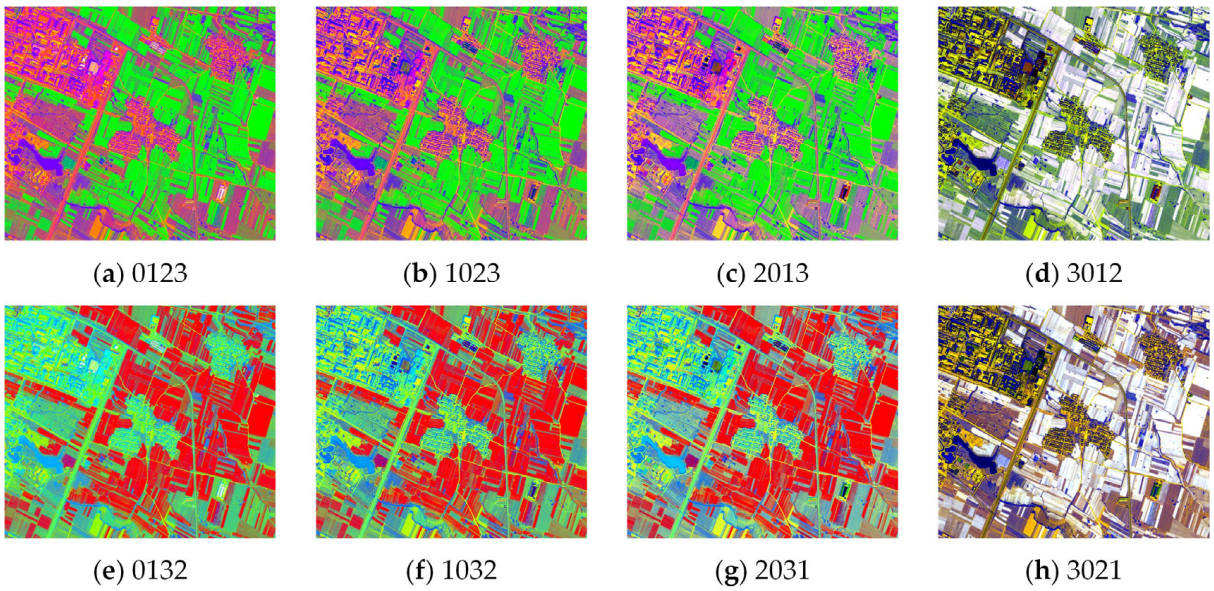

(**a**) 0123 (**b**) 1023 (**c**) 2013 (**d**) 3012

(**e**) 0132 (**f**) 1032 (**g**) 2031 (**h**) 3021

Figure A1. *Cont.*

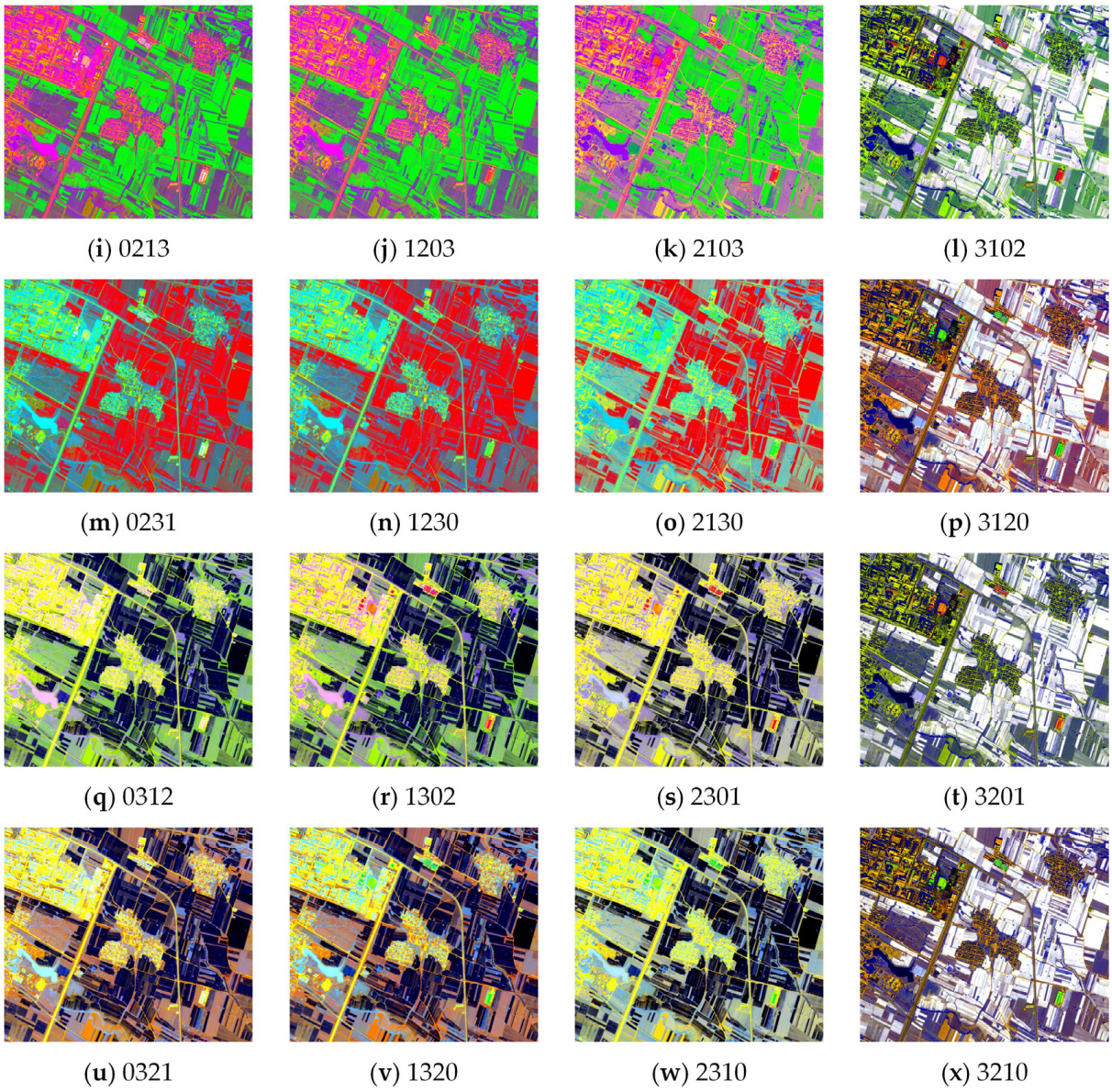

Figure A1. All combinations of the pseudo-TCT image of region 2. (**a**) 0123 combination image; (**b**) 1023 combination image; (**c**) 2013 combination image; (**d**) 3012 combination image; (**e**) 0132 combination image; (**f**) 1032 combination image; (**g**) 2031 combination image; (**h**) 3021-combination image; (**i**) 0213 combination image; (**j**) 1203-combination image; (**k**) 2103-combination image; (**l**) 3102-combination image; (**m**) 0231-combination image; (**n**) 1230-combination image; (**o**) 2130-combination image; (**p**) 3120-combination image; (**q**) 0312-combination image; (**r**) 1302-combination image; (**s**) 2301-combination image; (**t**) 3201-combination image; (**u**) 0321-combination image; (**v**) 1320-combination image; (**w**) 2310-combination image; (**x**) 3210-combination image.

References

1. Wiersma, D.J. *The Analytical Design of Spectral Measurements for Multispectral Remote Sensor Systems*; Purdue University: West Lafayette, IN, USA, 1979.
2. Markham, B.L.; Townshend, J.R.G. Land Cover Classification Accuracy as a Function of Sensor Spatial Resolution. In Proceedings of the International Symposium on Remote Sensing of Environment, Ann Arbor, MI, USA, 11–15 May 1981.
3. Hord, R.M. *Digital Image Processing of Remotely Sensed Data*; Elsevier: Amsterdam, The Netherlands, 1982.
4. Ahuja, S.N.; Biday, S. A Survey of Satellite Image Enhancement Techniques. *Int. J. Adv. Innov. Res. IJAIR* **2013**, *2*, 131–136.
5. Chien, C.-L.; Tsai, W.-H. Image Fusion with No Gamut Problem by Improved Nonlinear IHS Transforms for Remote Sensing. *IEEE Trans. Geosci. Remote Sens.* **2013**, *52*, 651–663. [CrossRef]

6. Bajpai, K.; Soni, R. Analysis of Image Enhancement Techniques Used in Remote Sensing Satellite Imagery. *Int. J. Comput. Appl.* **2017**, *975*, 8887. [CrossRef]
7. Zhao, J.; Wang, L.; Yang, H.; Wu, P.; Wang, B.; Pan, C.; Wu, Y. A Land Cover Classification Method for High-Resolution Remote Sensing Images Based on NDVI Deep Learning Fusion Network. *Remote Sens.* **2022**, *14*, 5455. [CrossRef]
8. Gu, L.; Cao, Q.; Ren, R. Building Extraction Method Based on the Spectral Index for High-Resolution Remote Sensing Images over Urban Areas. *J. Appl. Remote Sens.* **2018**, *12*, 045501. [CrossRef]
9. Yi, Z.; Jianhui, X. Impervious Surface Extraction with Linear Spectral Mixture Analysis Integrating Principal Components Analysis and Normalized Difference Building Index. In Proceedings of the 2016 4th International Workshop on Earth Observation and Remote Sensing Applications (EORSA), Guangzhou, China, 4–6 July 2016; pp. 428–432.
10. Zeng, Y.; Guo, Y.; Li, J. Recognition and Extraction of High-Resolution Satellite Remote Sensing Image Buildings Based on Deep Learning. *Neural Comput. Appl.* **2022**, *34*, 2691–2706. [CrossRef]
11. Kauth, R.J.; Thomas, G.S. The Tasselled Cap–a Graphic Description of the Spectral-Temporal Development of Agricultural Crops as Seen by Landsat. In Proceedings of the LARS Symposia, West Lafayette, IN, USA, 29 June–1 July 1976; p. 159.
12. Chen, C.; Fu, J.; Zhang, S.; Zhao, X. Coastline Information Extraction Based on the Tasseled Cap Transformation of Landsat-8 OLI Images. *Estuar. Coast. Shelf Sci.* **2019**, *217*, 281–291. [CrossRef]
13. Liu, Q.; Liu, G.; Huang, C. Monitoring Desertification Processes in Mongolian Plateau Using MODIS Tasseled Cap Transformation and TGSI Time Series. *J. Arid. Land* **2018**, *10*, 12–26. [CrossRef]
14. Chen, C.; Chen, H.; Liang, J.; Huang, W.; Xu, W.; Li, B.; Wang, J. Extraction of Water Body Information from Remote Sensing Imagery While Considering Greenness and Wetness Based on Tasseled Cap Transformation. *Remote Sens.* **2022**, *14*, 3001. [CrossRef]
15. Liu, Q.; Guo, Y.; Liu, G.; Zhao, J. Classification of Landsat 8 OLI Image Using Support Vector Machine with Tasseled Cap Transformation. In Proceedings of the 2014 10th International Conference on Natural Computation (ICNC), Xiamen, China, 19–21 August 2014; pp. 665–669.
16. Li, X.; Zhang, Y.; Luo, J.; Jin, X.; Xu, Y.; Yang, W. Quantification Winter Wheat LAI with HJ-1CCD Image Features over Multiple Growing Seasons. *Int. J. Appl. Earth Obs. Geoinf.* **2016**, *44*, 104–112. [CrossRef]
17. Chao, C.; Xinyue, H.E.; Jiaoqi, F.U.; Yanli, C.H.U. A Method of Flood Submerging Area Extraction for Farmland Based on Tasseled Cap Transformation from Remote Sensing Images. *J. Wuhan Univ. Inf. Sci. Ed.* **2019**, *44*, 1560–1566. [CrossRef]
18. Gillespie, A.R.; Kahle, A.B.; Walker, R.E. Color Enhancement of Highly Correlated Images. I. Decorrelation and HSI Contrast Stretches. *Remote Sens. Environ.* **1986**, *20*, 209–235. [CrossRef]
19. Robertson, P.K.; O'Callaghan, J.F. The Application of Perceptual Color Spaces to the Display of Remotely Sensed Imagery. *IEEE Trans. Geosci. Remote Sens.* **1988**, *26*, 49–59. [CrossRef]
20. Das, M.; Ghosh, S.K. Deep-STEP: A Deep Learning Approach for Spatiotemporal Prediction of Remote Sensing Data. *IEEE Geosci. Remote Sens. Lett.* **2016**, *13*, 1984–1988. [CrossRef]
21. Zheng, Z.; Tang, X.; Yue, Q.; Bo, A.; Lin, Y. Color Difference Optimization Method for Multi-Source Remote Sensing Image Processing. In Proceedings of the IOP Conference Series: Earth and Environmental Science; IOP Publishing: Bristol, UK, 2020; Volume 474, p. 042030.
22. Li, J.; Meng, L.; Yang, B.; Tao, C.; Li, L.; Zhang, W. LabelRS: An Automated Toolbox to Make Deep Learning Samples from Remote Sensing Images. *Remote Sens.* **2021**, *13*, 2064. [CrossRef]
23. Athar, S.; Wang, Z. A Comprehensive Performance Evaluation of Image Quality Assessment Algorithms. *IEEE Access* **2019**, *7*, 140030–140070. [CrossRef]
24. Wang, Z.; Bovik, A.C. Reduced-and No-Reference Image Quality Assessment. *IEEE Signal Process. Mag.* **2011**, *28*, 29–40. [CrossRef]
25. Chandler, D.M. Seven Challenges in Image Quality Assessment: Past, Present, and Future Research. *ISRN Signal Process.* **2013**, *2013*, 905685. [CrossRef]
26. Yin, G.; Wang, W.; Yuan, Z.; Han, C.; Ji, W.; Sun, S.; Wang, C. Content-Variant Reference Image Quality Assessment via Knowledge Distillation. *Proc. AAAI Conf. Artif. Intell.* **2022**, *36*, 3134–3142. [CrossRef]
27. Ponomarenko, N.; Lukin, V.; Zelensky, A.; Egiazarian, K.; Carli, M.; Battisti, F. TID2008-a Database for Evaluation of Full-Reference Visual Quality Assessment Metrics. *Adv. Mod. Radioelectron.* **2009**, *10*, 30–45.
28. Bosse, S.; Maniry, D.; Müller, K.-R.; Wiegand, T.; Samek, W. Deep Neural Networks for No-Reference and Full-Reference Image Quality Assessment. *IEEE Trans. Image Process.* **2017**, *27*, 206–219. [CrossRef] [PubMed]
29. Su, S.; Yan, Q.; Zhu, Y.; Zhang, C.; Ge, X.; Sun, J.; Zhang, Y. *Blindly Assess Image Quality in the Wild Guided by A Self-Adaptive Hyper Network–Supplementary Material*; Northwestern Polytechnical University: Xi'an, China, 2020.
30. Rehman, A.; Wang, Z. Reduced-Reference Image Quality Assessment by Structural Similarity Estimation. *IEEE Trans. Image Process.* **2012**, *21*, 3378–3389. [CrossRef] [PubMed]
31. Cheon, M.; Yoon, S.-J.; Kang, B.; Lee, J. Perceptual Image Quality Assessment with Transformers. In Proceedings of the IEEE/CVF Conference on Computer Vision and Pattern Recognition, Nashville, TN, USA, 20–25 June 2021; pp. 433–442.
32. Bosse, S.; Maniry, D.; Wiegand, T.; Samek, W. A Deep Neural Network for Image Quality Assessment. In Proceedings of the 2016 IEEE International Conference on Image Processing (ICIP), Phoenix, AZ, USA, 25–28 September 2016; IEEE: Phoenix, AZ, USA, 2016; pp. 3773–3777.

33. Liu, L.; Liu, B.; Huang, H.; Bovik, A.C. No-Reference Image Quality Assessment Based on Spatial and Spectral Entropies. *Signal Process. Image Commun.* **2014**, *29*, 856–863. [CrossRef]
34. Rollet, R.; Benie, G.B.; Li, W.; Wang, S.; Boucher, J.M. Image Classification Algorithm Based on the RBF Neural Network and K-Means. *Int. J. Remote Sens.* **1998**, *19*, 3003–3009. [CrossRef]
35. Lv, Z.; Hu, Y.; Zhong, H.; Wu, J.; Li, B.; Zhao, H. Parallel K-Means Clustering of Remote Sensing Images Based on Mapreduce. In Proceedings of the Web Information Systems and Mining: International Conference, WISM 2010, Sanya, China, 23–24 October 2010; Springer: Berlin/Heidelberg, Germany, 2010; pp. 162–170.
36. Lv, Z.; Liu, T.; Shi, C.; Benediktsson, J.A.; Du, H. Novel Land Cover Change Detection Method Based on K-Means Clustering and Adaptive Majority Voting Using Bitemporal Remote Sensing Images. *IEEE Access* **2019**, *7*, 34425–34437. [CrossRef]
37. Abbas, A.W.; Minallh, N.; Ahmad, N.; Abid, S.A.R.; Khan, M.A.A. K-Means and ISODATA Clustering Algorithms for Landcover Classification Using Remote Sensing. *Sindh Univ. Res. J.-SURJ Sci. Ser.* **2016**, *48*, 315–318.
38. Tong, X.-Y.; Xia, G.-S.; Lu, Q.; Shen, H.; Li, S.; You, S.; Zhang, L. Land-Cover Classification with High-Resolution Remote Sensing Images Using Transferable Deep Models. *Remote Sens. Environ.* **2020**, *237*, 111322. [CrossRef]
39. Liu, Q.; Liu, G.; Huang, C.; Xie, C. Comparison of Tasselled Cap Transformations Based on the Selective Bands of Landsat 8 OLI TOA Reflectance Images. *Int. J. Remote Sens.* **2015**, *36*, 417–441. [CrossRef]
40. Horne, J.H. A Tasseled Cap Transformation for IKONOS Images. In Proceedings of the ASPRS 2003 Annual Conference Proceedings, Anchorage, AK, USA, 5–9 May 2003.
41. Yang, M.; Jiao, L.; Liu, F.; Hou, B.; Yang, S. Transferred Deep Learning-Based Change Detection in Remote Sensing Images. *IEEE Trans. Geosci. Remote Sens.* **2019**, *57*, 6960–6973. [CrossRef]
42. Lian, R.; Wang, W.; Mustafa, N.; Huang, L. Road Extraction Methods in High-Resolution Remote Sensing Images: A Comprehensive Review. *IEEE J. Sel. Top. Appl. Earth Obs. Remote Sens.* **2020**, *13*, 5489–5507. [CrossRef]
43. Yuan, X.; Shi, J.; Gu, L. A Review of Deep Learning Methods for Semantic Segmentation of Remote Sensing Imagery. *Expert Syst. Appl.* **2021**, *169*, 114417. [CrossRef]
44. Rahaman, M.; Hillas, M.M.; Tuba, J.; Ruma, J.F.; Ahmed, N.; Rahman, R.M. Effects of Label Noise on Performance of Remote Sensing and Deep Learning-Based Water Body Segmentation Models. *Cybern. Syst.* **2022**, *53*, 581–606. [CrossRef]
45. Kazempour, D.; Beer, A.; Kroger, P.; Seidl, T. I Fold You so! An Internal Evaluation Measure for Arbitrary Oriented Subspace Clustering. In Proceedings of the 2020 International Conference on Data Mining Workshops (ICDMW), Sorrento, Italy, 17–20 November 2020; IEEE: Sorrento, Italy, 2020; pp. 316–323.

Disclaimer/Publisher's Note: The statements, opinions and data contained in all publications are solely those of the individual author(s) and contributor(s) and not of MDPI and/or the editor(s). MDPI and/or the editor(s) disclaim responsibility for any injury to people or property resulting from any ideas, methods, instructions or products referred to in the content.